High Power Laser Science and Engineering, (2024), Vol. 12, e81, 9 pages.
doi:10.1017/hpl.2024.59

HIGH POWER LASER SCIENCE AND ENGINEERING

RESEARCH ARTICLE

Quality assessment for large-aperture optical elements inducing phase jumps

Vicenţiu Iancu[1,2], Anda-Maria Talpoşi[1,2], Cristina Gheorghiu[1], Răzvan Ungureanu[3], Ioan Dăncuş[1], Dan-Gheorghiţă Matei[1], and Daniel Ursescu[1,2]

[1]*Extreme Light Infrastructure – Nuclear Physics (ELI-NP), Horia Hulubei National Institute for Physics and Nuclear Engineering, Măgurele, Romania*

[2]*Faculty of Physics, University of Bucharest, Măgurele, Romania*

[3]*National Institute for Laser, Plasma and Radiation Physics (INFLPR), Center for Advanced Laser Technologies (CETAL), Măgurele, Romania*

(Received 7 June 2024; revised 8 August 2024; accepted 28 August 2024)

Abstract

Achieving complex pulses with high-power lasers necessitates rigorous testing of specially designed optical components. The qualification of these components using complementary devices to access both the high-resolution and the large-aperture properties, followed by validation using propagation simulations, is proposed here. In particular, the topology of a large-aperture staircase-like Fresnel phase plate used to generate vortex pulses is qualified using a non-contact optical profiler and a large-aperture wavefront measurement setup based on a Shack–Hartmann sensor. The resulting topography is further used for simulating the focus of laser beams after passing through the phase plate. Step height distribution effects on the doughnut-shaped focus are identified, and avoiding the indicated pitfall in the design of the phase plate provides at least a 10-fold reduction of the irradiance modulation on the circumference of the focus in the super-Gaussian case.

Keywords: helical wavefront; large-aperture high-power lasers; optical profilometry; spiral phase plate; wavefront sensors

1. Introduction

Since the 1990s, significant progress has been made in the development of ultra-fast laser technology[1,2], with today's sources capable of producing peak output powers of the order of petawatts[3,4] and pulse duration of less than 10 femtoseconds (fs) from a relatively simple laser setup[5–8].

This is achieved through the use of broad-spectral-bandwidth pulses, which are amplified using the chirped pulse amplification (CPA) technique[9]. This new method has had a significant impact on both basic research and industrial applications, enabling the emergence of novel areas of science, such as high-energy-density physics[10,11], laboratory astrophysics[12–15], laser accelerators[16–18] and laser nuclear science[19,20], together with the exploration of previously inaccessible states of matter[21].

Over the last 30 years or more, the beam shape of high-irradiance lasers used in a wide range of applications has been characterized by an ideal flat-top beam, a Gaussian or super-Gaussian near-field fluence distribution, and a Gaussian-like focus. Nowadays, emerging techniques do not require standard Gaussian-like laser beams, but rather tailored spatial distributions in the far field (FF)[22], often generated by optical elements with phase jumps. In particular, the most basic light fields with a focal fluence shaped like a ring contain an optical vortex located at the beam's core. It is often modeled by Laguerre–Gaussian LG_{pl} beams[23] of radial index p and azimuthal order l, or modified versions, wherein the near-field irradiance distribution is transformed to a super-Gaussian profile to enhance energy extraction efficiency, in particular within laser chains.

Laguerre–Gaussian modes, known in the literature as helical beams, have a hollow irradiance profile and carry orbital angular momentum (OAM)[24]. An electromagnetic wave with OAM travels with a spiral-shaped wavefront, as opposed to the flat wave fronts that are typical of many high-powered lasers currently in use. Beams with a helical

Correspondence to: D.-G. Matei, Extreme Light Infrastructure – Nuclear Physics (ELI-NP), Horia Hulubei National Institute for Physics and Nuclear Engineering, 30 Reactorului, P. O. Box MG-6, 077125 Măgurele, Romania. Email: dan.matei@eli-np.ro

wavefront structure carry, in their cross-section, a specific set of points where the irradiance is zero and, as one traverses these points, the phase increases by the following:

$$\Delta\Phi = 2\pi l. \quad (1)$$

The non-zero integer l determines the topological charge of the helical surface.

The investigation of the characteristics of optical vortices has prospered following the publication of a comprehensive paper by Nye and Berry in 1974[25], which delineated the fundamental attributes of dislocations in wave trains. The study of generating and utilizing OAM laser beams has lately seen a significant increase in research; specifically, ring-shaped focus irradiance distributions have the potential to have numerous practical applications in high-intensity laser technology, utilizing OAM in the interaction processes[26]. This particular type of beams has already been applied in multiple domains, including particle confinement[27,28], optical communication[29], quantum computing[30], high-resolution microscopy[31,32] and astronomical observation[33–35].

Twisted helical phase beams are seen as a solution to enhance conventional ion acceleration[36] outcomes and as a potentially cost-effective alternative to circular polarization. This is because shaping the phase of a large-diameter laser beam is a more economical solution compared to modifying its polarization[37].

Despite the significant theoretical interest[38], there have been limited experimental studies[39] due to the difficulties encountered in generating and propagating large-aperture OAM beams in high-power laser systems (HPLSs). Nevertheless, despite the desirable features of doughnut-like beams, the efficacy of the experimental investigations has been hindered due to degradation of the irradiance pattern in the FF[40] and low damage thresholds and non-linearity effects induced by the propagating ultra-short laser pulses.

Ever since the first experimental generation of a beam with phase dislocation by Allen *et al.* in 1992[41], multiple techniques have been continuously developed and suggested[42,43]. The early methods focused on modifying the Gouy phase shift of the light beam, converting the arbitrary orders of Hermite–Gaussian modes into Laguerre–Gaussian modes by a pair of cylindrical lenses[44]. Later on, classical approaches included continuous[45,46] and discrete[47–51] optical elements, computer-generated holograms[52], digital devices (spatial light modulators (SLMs)[53] and digital mirror devices (DMDs)[54]), more recent schemes such as metasurfaces[55] and even s/q-plates[56–58]. In most applications, these techniques use conventional small-diameter optical elements with phase jumps, as compared to large-size devices that present technological challenges either in manufacturing or when implemented in experiments.

As the use of OAM focal spot irradiance distributions gains growing interest, accurate manufacturing and qualification of versatile and diverse optical elements inducing wavefront dislocations are required.

The goal of this paper is to identify proper ways to qualify large-aperture optical elements inducing phase jumps. In this respect, three complementary methods are combined. Firstly, optical component discontinuities are mapped with high lateral resolution using non-contact optical profilometry. Then, the useful aperture of the optical phase plate is characterized using a setup based on a wavefront sensor. Finally, the obtained information is used as input for the simulation of propagation and compared with the ideal pattern of the field generated when no distortions are present. To properly illustrate this, we present the challenges and results related to high-resolution wavefront characterization of pulses generated with a large-diameter helical staircase-like phase plate (SPP).

The paper is structured as follows. In Section 2, we present the method to generate vortex waves and the tools used to qualify them: profilometry, wavefront sensing and the simulation approach implemented. The results concerning the characterization of the large-aperture optical component are presented in Section 3. Subsequently, in Section 4 we use the result as input for the propagation towards the focus of an ideal super-Gaussian or a real measured beam and compare the outcomes of various scenarios. The conclusions are presented in Section 5.

2. Methods

A laser beam with a flat wavefront passes through an uncoated phase plate with a diameter of 150 mm and thickness of 2.3 mm to acquire OAM. The choice of a flat wavefront is motivated by the fact that the experimental setups usually include a deformable mirror (DM) to compensate deviations from flatness. In the FF, the beam is expected to produce an annular field distribution. The phase plate, specified by the producer company for 800 nm and $l = 1$ in transmission, single-pass configuration, was manufactured from fused silica (FS) with one of the optically active surfaces having a topography similar to a spiral staircase. The staircase profile was obtained by lithographic methods and reactive ion etching (RIE). The design is such that the light that passes through the pair of steps with the highest height difference acquires a phase delay equivalent to one wavelength, according to Equation (1), due to the retardation when propagating through the material.

A comprehensive characterization of the topography involves at least two measurements. The first one should obtain the heights of all the steps that comprise the staircase. The second measurement determines the slowly varying background arising from the imperfection in the flatness of the substrate used for the phase plate.

The step height distribution was statistically measured by optical profilometry using a Sensofar S neox profiler,

https://doi.org/10.1017/hpl.2024.59 Published online by Cambridge University Press

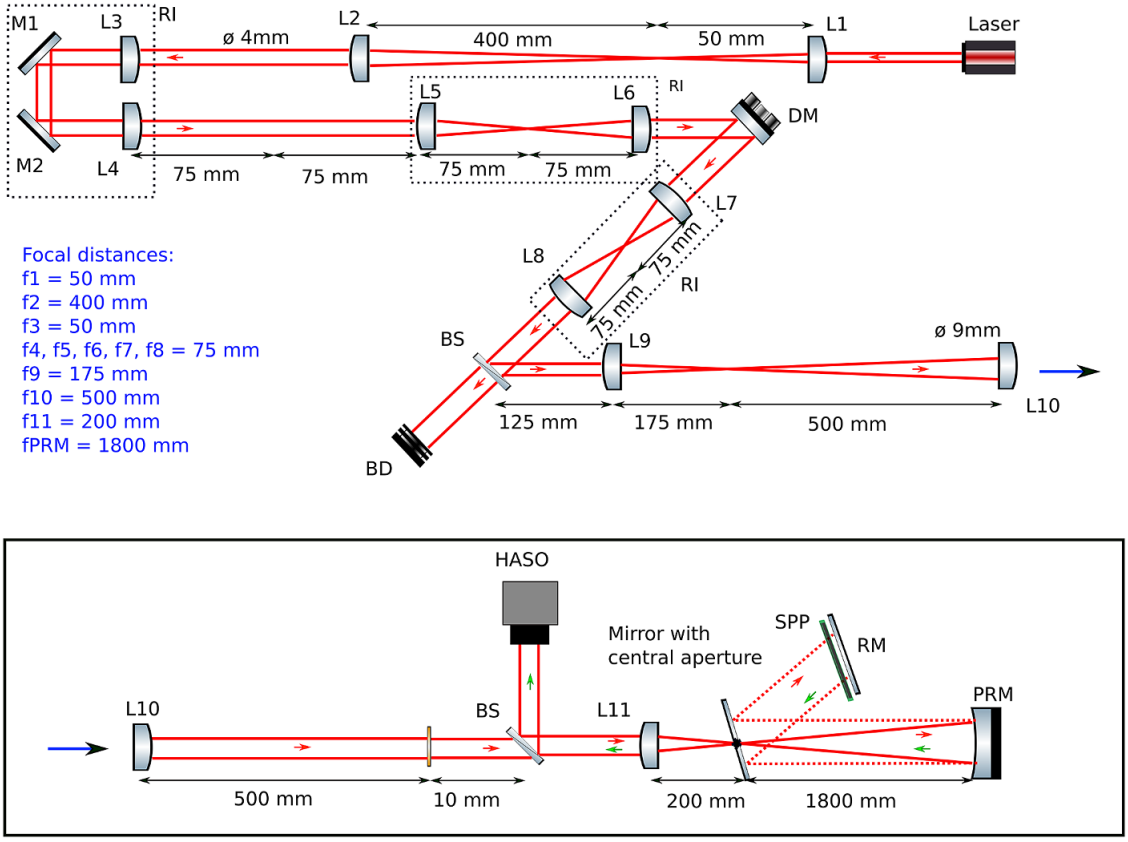

Figure 1. Schematic representation of the experimental setup used to generate Laguerre–Gaussian beams and characterize diffractive optical elements. The fundamental Gaussian beam, emitted by a He-Ne laser source ($\lambda = 632.8$ nm, $P = 5$ mW), was relay imaged and collimated onto an SPP, transformed into an optical vortex and detected by a high-resolution S-H wavefront sensor (HASO4 126 VIS, Imagine Optics, number of sub-pupils 126×172, pupil size $10.2\,\text{mm} \times 13.8\,\text{mm}$, 3×12 bit RGB color depth) placed in the Fourier plane of the SPP element. RI, collimating relay imaging system; L1–L11, plano-convex lenses; M1, M2, plane mirrors; DM, deformable mirror; BS, beam splitter; BD, beam dump; HASO, wavefront sensor; PRM, on-axis parabolic mirror; SPP, spiral phase plate; RM, reference plane mirror. The values f1–f11 and fPRM are the focal lengths of lenses L1–L11 and of the PRM.

specified with an uncertainty of 4 nm for a step height standard of 186 nm. Since RIE can achieve a depth uniformity of a few percent, with the largest deviations occurring close to the edges of the patterned area, the center was deemed representative for the height distribution across the aperture of interest.

Measuring the deviation from a perfectly flat substrate with the optical profiler is not practical and is error-prone, since it requires stitching together a large number of images acquired over days or weeks. It can be done instead by sending a flat wavefront through the phase plate and measuring the result with a Shack–Hartmann (S-H) sensor. As shown in Figure 1, the experimental setup comprises a collimated beam generation system and an S-H sensor.

A coherent, linearly polarized, continuous ($\text{TEM}_{00} > 99\%$) light beam, emitted by a He-Ne laser source (REO, Model 31005) of central wavelength 632.8 nm, 5 mW power and 0.8 mm beam diameter, is used. The Gaussian beam is expanded and collimated through a series of $4f$-configuration relay imaging systems and telescopes. The geometry of the beam expanders enables, in the first place, the preservation of the beam properties during transport throughout the optical system and, secondly, provides the capability to measure with different apertures, up to approximately equal to 10 cm.

A flexible bimorph piezoelectric DM (Boston Micromachines, model Multi-DM DM140A-35-IM01, active array size 12×12 actuators, Au-coated material, stroke 3.5 μm, active aperture $4.4\,\text{mm} \times 4.4\,\text{mm}$) was used in a factory-flat configuration.

The experimental setup allows for the samples to be placed at different locations, in transmission or in reflection, thus enabling wavefront qualifications at different apertures. The residual wavefront error of the complete system is subtracted from the actual qualification measurement of the phase plate. The SPP was illuminated in a double-path transmission geometry in the Fourier plane of the wavefront sensor. The recorded wavefront data were divided by 2 in order to obtain the actual distortion induced by the phase plate when used in an experiment. The smallest possible distance between the SPP and reference plane mirror (RM) (≈2 mm) was used in order to minimize the wavefront measurement

https://doi.org/10.1017/hpl.2024.59 Published online by Cambridge University Press

error, but small measurement uncertainties do not change the conclusion of the present study. As the incident beam passes through the surface of the phase plate, it undergoes a transformation from a fundamental Gaussian beam to a vortex beam.

To evaluate the quality of the phase discontinuity of the light field generated by the vortex element and the propagation characteristics, we measured the resultant waveform. A high-resolution wavefront sensor (HASO4 126 VIS) was used. It consists of 126 × 172 sub-pupils and it has an aperture size of 10.2 mm × 13.8 mm. The sensor is placed on an *XYZ* translational stage in the conjugated plane of the laser source and the DM. The concept used to increase sampling density is based on the linearized focal plane technique (LIFT)[59,60], which performs a phase retrieval algorithm on each micro-lens image.

The best-fit third-degree polynomial surface was determined from the measured wavefront over a diameter of 70 mm. The height distribution of the steps, superposed on the polynomial function, was used to simulate the propagation of the beam in the FF. The results were compared with the propagation through an ideal plate, where the steps have equal heights and the substrate is perfectly flat. The simulations were done using the package LightPipes for Python by calculating the Fresnel–Kirchhoff integrals.

For the initial field distribution, two types of data were used. Firstly, a super-Gaussian function of the eighth order with radial symmetry was calculated (for a discussion of super-Gaussians of different orders see Ref. [61]). Secondly, the beam profile of the 100 TW HPLS (the HPLS of the Extreme Light Infrastructure – Nuclear Physics (ELI-NP) facility) output[3] recorded on 26 November 2022 was applied, for a wavelength of 800 nm in air. The analysis is restricted to narrow-bandwidth pulses and the optical component quality at the central wavelength. It has been shown[48] that even for a bandwidth of 10% of the central wavelength, the conversion efficiency to a vortex beam drops by only a few percent compared with the monochromatic case. For rigorous results, the analysis of the wavefront should be extended to include full spatial-temporal description[62,63].

The quantitative evaluation of the ring pattern in focus was done by computing a circular section of the irradiance[40]. The radius of the circular section was the one where the azimuthally integrated radial profile had the highest value. The focus quality was tied to the coefficient of variation (CV) or the relative standard deviation (RSD) of the circular section, using the following formula:

$$\mathrm{CV} = \frac{\sigma}{\mu}, \tag{2}$$

with σ being the standard deviation and μ the mean value of the section. A flat profile or perfect focus corresponds to 0% RSD. Complementarily, the quality of the helical beam focal spot was monitored using the azimuthal integration of the doughnut.

3. Phase plate characterization

The topography of the central section with an area of 10 mm × 10 mm of the phase plate was measured with the optical profiler. This was necessary for assessing whether the step heights were equal, as required in the ideal SPP case. The topography, shown in Figure 2, was obtained by stitching more than 2300 smaller, overlapping scans of the surface.

The curved background of the image hinders the calculation of the step height distribution. For background removal, the gradient of the surface was first calculated. The discontinuities in the gradient image generated at the step borders were then replaced by interpolating between the neighboring areas. Finally, the background was obtained by integrating the filtered gradient image.

The height distribution was obtained using a Gaussian kernel density estimator (KDE) on the image data without the background. A KDE was preferred over a histogram because the maximum of the latter depends on the choice of bin size and starting position. For each data point, the KDE method adds up the values of a kernel function (in this case a Gaussian) centered at that point. The resulting sum is an estimate of the distribution function.

For extracting the average heights of the steps, the result of the KDE was fitted with the sum of 15 Gaussian functions (not related to the kernel of the KDE), corresponding to the intermediate step heights, where the centers of the Gaussians are allowed to vary during the fitting process.

The maximum height difference across the phase plate is 1.754 μm. For FS (refractive index $n = 1.4534$ at $\lambda = 795$ nm), this yields a maximum phase shift of 2π (one wavelength optical path difference), for a beam with an initially flat wavefront. The 2π phase shift is considered also in the design of helical phase plates in reflection[64]. It should

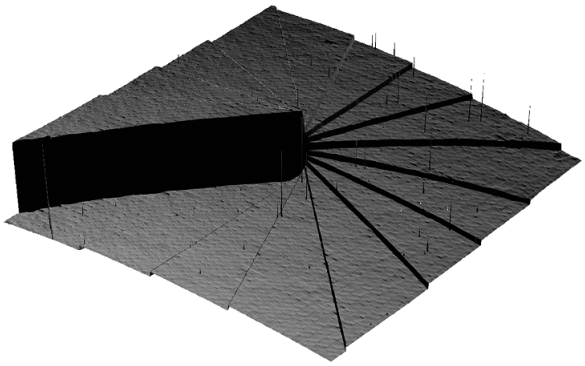

Figure 2. A 10 mm × 10 mm optical profiler image with a height range of 3 μm. The height was exaggerated to observe the curved background and the stitching artifacts.

https://doi.org/10.1017/hpl.2024.59 Published online by Cambridge University Press

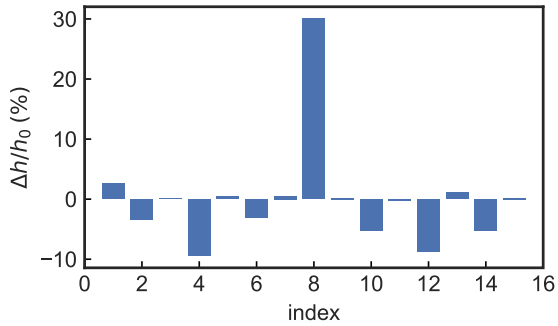

Figure 3. Relative error of the step heights across the phase plate, compared with the average value.

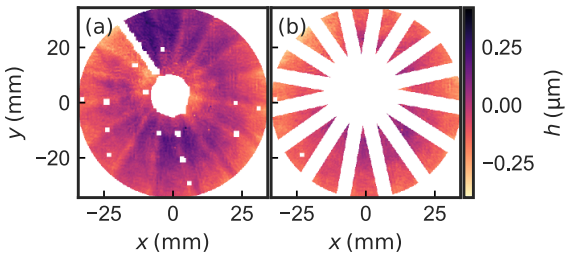

Figure 4. Wavefront distortion as measured with the Shack–Hartmann setup: (a) initial wavefront; (b) wavefront after masking out the discontinuities.

be noted that each of the 16 terraces of the SPP corresponds to a constant phase of the wavefront.

Assuming 15 equal step heights, the maximum height of 1.754 μm should yield a single step height of 116.9 nm. This value, as well as the overall step height, is close to that proposed by Sueda *et al.*[47], also using an FS plate in transmission. The measured step heights have the same average value but with a standard deviation of 14.7 nm. They range between 101 and 167 nm, with the largest gap occurring between the eighth and the ninth steps. The distribution of the height error to the mean is shown in Figure 3.

The complementary analysis of the wavefront was performed over a 70 mm central aperture. This was required as it is known that thin optical components often introduce residual wavefront distortions (RWDs) as a consequence of imperfect polishing of the surfaces. Figure 4(a) shows the wavefront measurement result. The RWD was estimated in the form of a polynomial obtained from the wavefront measured with the S-H setup by first masking out the discontinuities generated at the step boundaries using the wavefront sensor's software (Figure 4(b)). The resulting surface is approximated with a coefficient of determination $R^2 = 0.81$ by the following function:

$$f(x,y) = 10^{-2} \sum_{i,j=0}^{3} a_{i,j} x^i y^j, \tag{3}$$

with $a_{i,j}$ being the elements of the matrix:

$$\begin{pmatrix} a_{0,0} & 3.24 & -1.50 & -0.164 \\ 2.59 & -0.250 & -0.111 & 0.014 \\ -2.11 & -0.029 & -0.103 & 0.046 \\ -0.244 & 0.036 & 0.093 & -0.039 \end{pmatrix}, \tag{4}$$

where x, y are in centimeters, $f(x,y)$ is in micrometers and the center of the phase plate is in the origin. The value of $a_{0,0}$ is irrelevant since it only adds a piston term to the phase.

4. Impact of staircase-like phase plate imperfections on focus

For beam propagation simulations, a square region with a size of 150 mm and a lateral resolution of 2501 pixels was used. Figure 5(a) shows the eighth-order super-Gaussian irradiance distribution, with a full-width at half-maximum of 48.5 mm and wavelength 795 nm, and the 100 TW HPLS output irradiance pattern (Figure 5(b)). The staircase-like phase distribution is shown in Figure 5(c). The polynomial background from Equation (3), in units of wavelength, is shown in Figure 5(d).

For the first set of simulations, a spiral phase filter, with the distribution of step heights as measured with the profiler (Figure 3) and having the polynomial background given by Equation (3), was applied to the super-Gaussian and HPLS fields. The resulting field was propagated for a distance of 40 m to a perfect lens with a focal distance of 150 mm. The irradiance distribution was then calculated in the back focal plane of the lens, where the computed square region

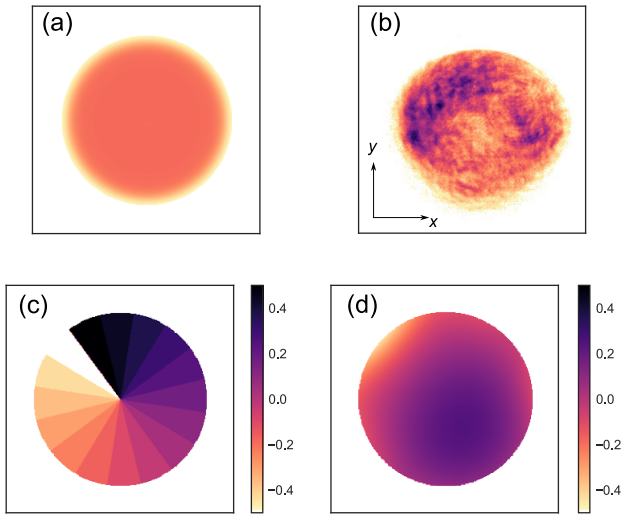

Figure 5. Starting field distribution of irradiance (a), (b) and equi-distributed phase (c). Image (d) shows the phase distortion corresponding to the fitted polynomial. The squares have a size of 80 mm. The irradiance distributions in (a) and (b) are normalized to the same power and share the same intensity scale. The unit of phase distributions is one wavelength.

https://doi.org/10.1017/hpl.2024.59 Published online by Cambridge University Press

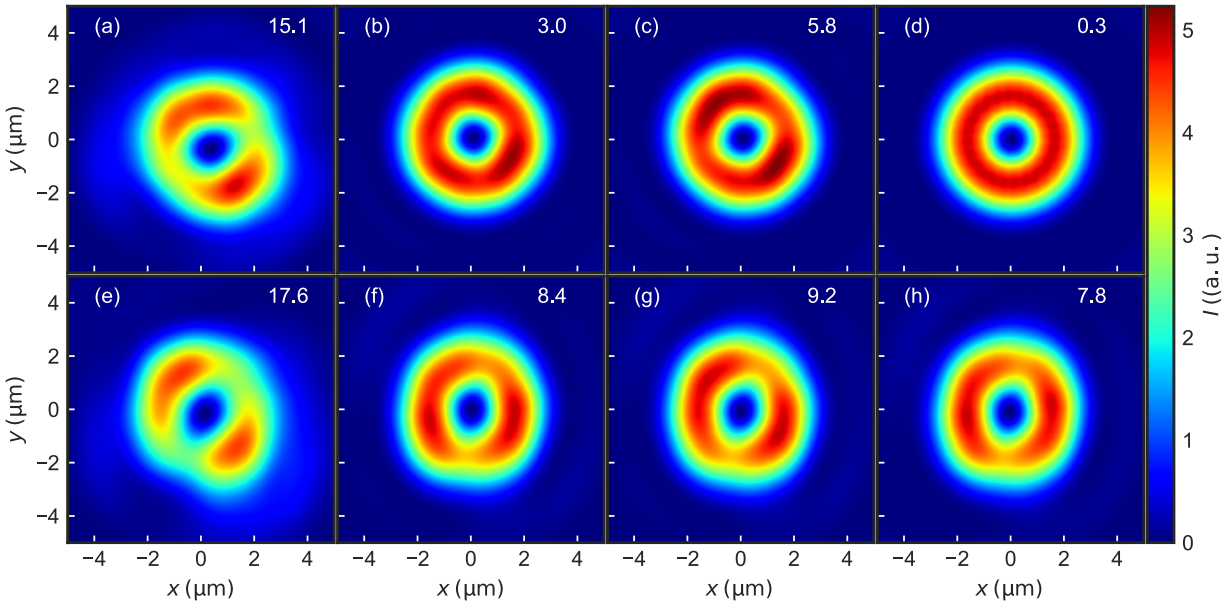

Figure 6. Simulated irradiance profiles in focus and the relative standard deviation (in percent RSD) of the circular sections through the points with the highest value. The 2π phase jump in the initial phase distribution was, for all images calculated, in the upper left quadrant, at an angle of 36.6° with the vertical. The rows index the initial spatial distribution of the field: super-Gaussian (a)–(d) or measured in the HPLS (e)–(h). The columns index the step height distribution across the spiral: nonuniform as measured, with the wavefront background being polynomial (a), (e) or flat (b), (f); uniform between the total height difference measured (c), (g); uniform, with corrected total height (d), (h). For the last two columns, no polynomial distortion of the wavefront was applied. The images share the same range of values for the color map.

size reached a value of 22 μm. Values of 15.1% RSD and 17.6% RSD of the circular section were obtained for a super-Gaussian beam and the HPLS beam, respectively (see Figures 6(a) and 6(e)). If the phase filter has a flat background instead, the values drop by about 10% RSD and the focal spot becomes more annular, as shown in Figures 6(b) and 6(f).

For further refining the focus quality, the step height distribution was considered to be uniform. Neither the super-Gaussian nor the HPLS beam achieved a better focal pattern (Figures 6(c) and 6(g)), and a modulation in the ring shape remains, even for the perfect super-Gaussian field.

Trying to pinpoint the source of the remaining modulation, it was realized that it lies in the distribution of step heights across the staircase. There are two possibilities of approximating a continuous phase plate with a uniformly stepped structure. In the first case, shown in Figure 7(a), which corresponds to the SPP as measured with the optical profiler, the largest phase jump corresponds indeed to one wavelength as for a continuous plate. To simplify the drawing, a four-step SPP was considered. The phase, however, is not uniformly distributed, because the phases on the first and last steps are equivalent, being one wavelength apart, thus effectively doubling the area of the zero phase-shift step. The correct step height distribution (Figure 7(b)), as presented also in the work of Longman *et al.*[50], results in a phase plate whose overall height is lower than for a continuous plate. The difference comes from the last step of height $l\lambda/N$ which, as seen in Figure 7(b), is 'virtual'. It follows that the previously

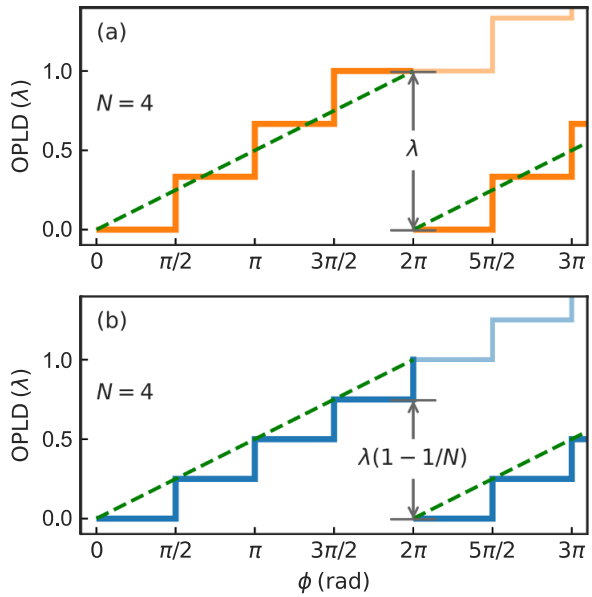

Figure 7. Two ways of approximating a continuous phase plate of $l = 1$ (dashed green line) with a discrete, $N = 4$-step plate (orange in (a) and blue in (b)) and the resulting optical path length difference (OPLD) as a function of the azimuth ϕ. The largest phase jump is λ in (a), but in (b) it is $\lambda(1 - 1/N)$.

determined height of 1.754 μm should be divided between 16 equal steps, instead of 15; hence the heights of the steps for the next simulations were decreased by 7.3 nm, from 116.9 to 109.6 nm.

https://doi.org/10.1017/hpl.2024.59 Published online by Cambridge University Press

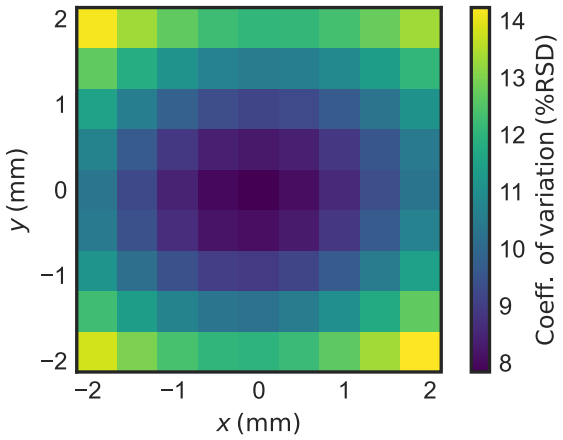

Figure 8. Coefficient of variation of the circular section in the focus as a function of the relative lateral shift between the phase plate and the HPLS beam.

The CV for the super-Gaussian beam was thus reduced to 1.5% RSD, a value limited by aliasing and diffraction at the simulated field boundaries. With 8001-pixel resolution and the initial space size of 600 mm, the RSD of the circular section in focus is only 0.3% (Figure 6(d)).

In practice, however, the doughnut focus quality for the HPLS beam is limited by the nonuniform cross-sectional irradiance distribution. Even with the correct distribution of the step heights, the focus quality remains at 7.8% RSD (Figure 6(h)). It should be noted that an incorrectly distributed step height like that in Figure 7(a) is, in effect, a phase plate that acts correctly at a different (longer) wavelength. Equivalently, it can be considered as having a non-integer charge for the working wavelength. For the investigated SPP, the correct wavelength would be 847 nm.

When performing the propagation simulations, the angular position of the largest phase jump in the spiral phase distribution was chosen arbitrarily, avoiding multiples of $\pi/2$. It was set at an azimuth of 126.6°, like in Figures 4(a) and 5(c). Any asymmetry resulting from a nonuniform irradiance distribution of the starting field, like in Figure 5(b), or from a non-integer charge[48], can be partially compensated with a lateral displacement of the phase mask. The position of the phase mask was therefore chosen to be the one that gives the minimum value of the RSD in focus. As an example, Figure 8 shows the dependency of the RSD value on the displacement for a flat background phase mask with step height distribution as measured with the profiler (Figure 6(f)). It can be approximated by a quadratic two-dimensional polynomial up to a relative root mean square of residuals of 0.13%. The optimization of the phase mask position was done for all the cases considered. The figure also shows the sensitivity, about 0.4 mm, of the doughnut quality with respect to the position of the phase plate.

The circular profiles obtained at the radius of maximum value for the azimuthally integrated irradiance profiles are shown in Figure 9(a). The best scenario (super-Gaussian, flat wavefront, optimized step heights) is depicted by the curve denoted Figure 6(d). The low-amplitude, fast modulations present in the profile are coming from numerical noise, due to the limited size and resolution of the computed input field, and set the limit of calculations. For the other three cases (Figures 6(b), 6(e) and 6(h)) analyzed in Figure 9, slower modulations are observed. For the Figure 6(b) case (super-Gaussian, measured nonuniform steps), the associated modulation is 3%, while for the Figure 6(h) case (measured beam profile, optimized step heights) the modulation is higher at 7.8%. When adding the polynomial wavefront to nonuniform steps and a measured beam profile, the RSD is 17.6%. It should be noted that a DM can compensate the wavefront background, leading to an achievable RSD of 8.4% (Figure 6(f)).

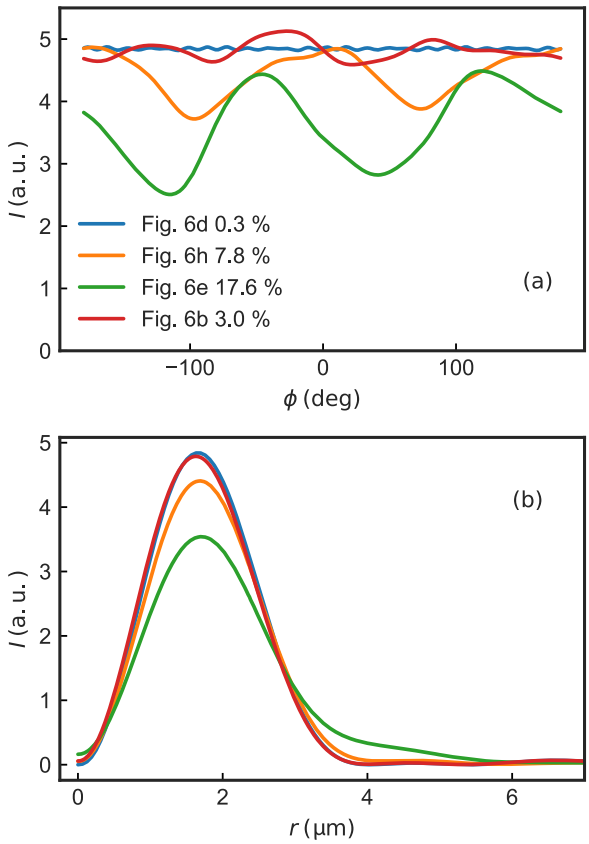

Figure 9. Circular sections (a) through the irradiance profiles in focus for several cases, and azimuthal integration (b) of the respective profiles. The legend refers to the images from Figure 4 and their respective RSDs.

The azimuthally integrated irradiance profiles are shown in Figure 9(b). One can observe the overall decrease in the irradiance across the ring, more than 30%, in the worst case analyzed (Figure 6(e)). This can significantly impact the estimated particle acceleration processes[37]. Analyzing the polynomial background of the wavefront and removing it using a DM would lead to a higher quality doughnut focus. Both can be achieved, for example, using the ZEHBRO

https://doi.org/10.1017/hpl.2024.59 Published online by Cambridge University Press

method[40]. Comparing the cases in Figures 6(b) and 6(d) in Figure 9(b) shows that the step height distribution does not impact significantly the integrated peak irradiance around the ring. A nonuniform irradiance profile of the laser, however, with or without the wavefront background, illustrated respectively in Figures 6(e) and 6(h), leads to a significant decrease in the irradiance. This decrease can be used to quantify the doughnut quality, like the Strehl ratio in the case of vortex-free pulses.

A final remark is related to the depth of the doughnut hole, which was indicated as a signature of distortions in the case of helical pulses with spatial-temporal couplings[63]. The relative depth of the hole in the worst-case scenario (see Figure 9(b)) is only 4%, making it difficult to distinguish in experiments.

5. Conclusions

In this paper, a qualification method for large-aperture optical elements inducing phase jumps has been proposed, and is of great interest in applications such as laser-driven charged particle acceleration and optical metrology. The method is based on three complementary approaches: high-resolution topography of the optical component, large-aperture characterization of the useful wavefront and numerical propagation of the reference laser pulse to the Fourier plane using the gathered information. To illustrate the method, we considered the case of a large-aperture, 16-step vortex phase plate, in the context of the 100 TW output from the HPLS.

Unexpected, non-negligible variations in the step heights of the phase plate and also a flaw in the design, related to the overall phase jump for the chosen wavelength, were identified using high-resolution optical profilometry. The low-resolution, high-aperture wavefront determination allowed one to take into account the residual low-order wavefront distortions on the overall focus of the pulses. Further, propagation code based on Fresnel–Kirchhoff integrals was used to assess the modification of the focus after the measured phase plate, including the positioning accuracy of the phase plate in order to minimize the RSD of the modulation. When using a super-Gaussian beam, the impact on the focus of each of the observed characteristics above could be quantified.

Furthermore, the deleterious effects of amplitude modulations in the used beam profile were studied. Two parameters were identified for practical use. The irradiance modulation around the doughnut profile in the focus, also used in the ZEHBRO technique[40], affects the symmetry of the interaction of the laser with the target. The azimuthal integration of the focused pulses shows that the peak irradiance suffers a significant decrease of more than 30% when compared with the optimized case. It is mostly introduced by the residual wavefront background.

Applying this method to the large-aperture discrete optical phase plate shows that the efforts in improving the quality of the optical component have to be doubled by the proper control of not only the beam wavefront, but also the beam irradiance modulations in the near-field in order to achieve the highest irradiance in focus.

Acknowledgements

This work was realized through the ‘Nucleu’ program, funded by the Romanian Ministry for Education and Research, project number PN 23 21 01 05 Faza 3 (II), and supported through IOSIN ‘Sistem Laser De Mare Putere (HPLS) Şi Laborator Optică IFIN-HH / ELI-NP’, through CNCS-UEFISCDI (PN-IIIP4-ID-PCCF-2016–0164), through EU-H2020 871161 (IMPULSE) and by ELI-NP Phase II, a project co-financed by the Romanian Government and the European Union through the European Regional Development Fund and the Competitiveness Operational Programme (1/07.07.2016, COP, ID 1334) and Project ELI-RO/DFG/2023˙001 ARNPhot funded by the Institute of Atomic Physics Romania.

References

1. M. M. Murnane, H. C. Kapteyn, and R. W. Falcone, Phys. Rev. Lett. **62**, 155 (1989).
2. S. Backus, C. G. Durfee III, M. M. Murnane, and H. C. Kapteyn, Rev. Sci. Instrum. **69**, 1207 (1998).
3. F. Lureau, G. Matras, O. Chalus, C. Derycke, T. Morbieu, C. Radier, O. Casagrande, S. Laux, S. Ricaud, G. Rey, A. Pellegrina, C. Richard, L. Boudjemaa, C. Simon-Boisson, A. Baleanu, R. Banici, A. Gradinariu, C. Caldararu, B. D. Boisdeffre, P. Ghenuche, A. Naziru, G. Kolliopoulos, L. Neagu, R. Dabu, I. Dancus, and D. Ursescu, High Power Laser Sci. Eng. **8**, e43 (2020).
4. C. Radier, O. Chalus, M. Charbonneau, S. Thambirajah, G. Deschamps, S. David, J. Barbe, E. Etter, G. Matras, S. Ricaud, V. Leroux, C. Richard, F. Lureau, A. Baleanu, R. Banici, A. Gradinariu, C. Caldararu, C. Capiteanu, A. Naziru, B. Diaconescu, V. Iancu, R. Dabu, D. Ursescu, I. Dancus, C. A. Ur, K. A. Tanaka, and N. V. Zamfir, High Power Laser Sci. Eng. **10**, e21 (2022).
5. M. D. Perry and G. Mourou, Science **264**, 917 (1994).
6. J. Zhou, I. P. Christov, G. Taft, C.-P. Huang, M. M. Murnane, and H. C. Kapteyn, Opt. Lett. **19**, 1149 (1994).
7. M. Nisoli, S. D. Silvestri, O. Svelto, R. Szipöcs, K. Ferencz, C. Spielmann, S. Sartania, and F. Krausz, Opt. Lett. **22**, 522 (1997).
8. G. Mourou, N. Fisch, V. Malkin, Z. Toroker, E. Khazanov, A. Sergeev, T. Tajima, and B. L. Garrec, Opt. Commun. **285**, 720 (2012).
9. D. Strickland and G. Mourou, Opt. Commun. **55**, 447 (1985).
10. D. Hoffmann, A. Blazevic, P. Ni, O. Rosmej, M. Roth, N. Tahir, A. Tauschwitz, S. Udrea, D. Varentsov, K. Weyrich, and Y. Maron, Laser Particle Beams **23**, 47 (2005).
11. R. P. Drake, in *Shock Wave and High Pressure Phenomena* (Springer, 2006), pp. 1–17.
12. B. A. Remington, R. P. Drake, H. Takabe, and D. Arnett, Phys. Plasmas **7**, 1641 (2000).
13. B. A. Remington, R. P. Drake, and D. D. Ryutov, Rev. Mod. Phys. **78**, 755 (2006).

https://doi.org/10.1017/hpl.2024.59 Published online by Cambridge University Press

14. H.-S. Park, D. Ryutov, J. Ross, N. Kugland, S. Glenzer, C. Plechaty, S. Pollaine, B. Remington, A. Spitkovsky, L. Gargate, G. Gregori, A. Bell, C. Murphy, Y. Sakawa, Y. Kuramitsu, T. Morita, H. Takabe, D. Froula, G. Fiksel, F. Miniati, M. Koenig, A. Ravasio, A. Pelka, E. Liang, N. Woolsey, C. Kuranz, R. Drake, and M. Grosskopf, High Energy Density Phys. **8**, 38 (2012).
15. A. Casner, T. Caillaud, S. Darbon, A. Duval, I. Thfouin, J. Jadaud, J. LeBreton, C. Reverdin, B. Rosse, R. Rosch, N. Blanchot, B. Villette, R. Wrobel, and J. Miquel, High Energy Density Phys. **17**, 2 (2015).
16. T. Tajima and J. M. Dawson, Phys. Rev. Lett. **43**, 267 (1979).
17. V. Malka, J. Faure, Y. A. Gauduel, E. Lefebvre, A. Rousse, and K. T. Phuoc, Nat. Phys. **4**, 447 (2008).
18. S. M. Hooker, Nat. Photonics **7**, 775 (2013).
19. D. Umstadter, Phys. Plasmas **8**, 1774 (2001).
20. K. W. D. Ledingham, P. McKenna, and R. P. Singhal, Science **300**, 1107 (2003).
21. R. W. Schoenlein, W. P. Leemans, A. H. Chin, P. Volfbeyn, T. E. Glover, P. Balling, M. Zolotorev, K.-J. Kim, S. Chattopadhyay, and C. V. Shank, Science **274**, 236 (1996).
22. H. Rubinsztein-Dunlop, A. Forbes, M. V. Berry, M. R. Dennis, D. L. Andrews, M. Mansuripur, C. Denz, C. Alpmann, P. Banzer, T. Bauer, E. Karimi, L. Marrucci, M. Padgett, M. Ritsch-Marte, N. M. Litchinitser, N. P. Bigelow, C. Rosales-Guzmán, A. Belmonte, J. P. Torres, T. W. Neely, M. Baker, R. Gordon, A. B. Stilgoe, J. Romero, A. G. White, R. Fickler, A. E. Willner, G. Xie, B. McMorran, and A. M. Weiner, J. Opt. **19**, 013001 (2016).
23. F. Pampaloni and J. Enderlein, arXiv:physics/0410021 (2004).
24. M. J. Padgett, Opt. Express **25**, 11265 (2017).
25. J. F. Nye and M. V. Berry, Proc. Roy. Soc. London A **336**, 165 (1974).
26. J. Vieira and J. Mendonça, Phys. Rev. Lett. **112**, 215001 (2014).
27. A. T. O'Neil, I. MacVicar, L. Allen, and M. J. Padgett, Phys. Rev. Lett. **88**, 053601 (2002).
28. M. Padgett and R. Bowman, Nat. Photonics **5**, 343 (2011).
29. A. E. Willner, H. Huang, Y. Yan, Y. Ren, N. Ahmed, G. Xie, C. Bao, L. Li, Y. Cao, Z. Zhao, J. Wang, M. P. J. Lavery, M. Tur, S. Ramachandran, A. F. Molisch, N. Ashrafi, and S. Ashrafi, Adv. Opt. Photonics **7**, 66 (2015).
30. A. Mair, A. Vaziri, G. Weihs, and A. Zeilinger, Nature **412**, 313 (2001).
31. B. J. McMorran, A. Agrawal, I. M. Anderson, A. A. Herzing, H. J. Lezec, J. J. McClelland, and J. Unguris, Science **331**, 192 (2011).
32. M. Ritsch-Marte, Philos. Trans. Roy. Soc. A **375**, 20150437 (2017).
33. G. C. G. Berkhout and M. W. Beijersbergen, Phys. Rev. Lett. **101**, 100801 (2008).
34. M. Harwit, Astrophys. J. **597**, 1266 (2003).
35. M. P. J. Lavery, F. C. Speirits, S. M. Barnett, and M. J. Padgett, Science **341**, 537 (2013).
36. S. Busold, A. Almomani, V. Bagnoud, W. Barth, S. Bedacht, A. Blažević, O. Boine-Frankenheim, C. Brabetz, T. Burris-Mog, T. Cowan, O. Deppert, M. Droba, H. Eickhoff, U. Eisenbarth, K. Harres, G. Hoffmeister, I. Hofmann, O. Jaeckel, R. Jaeger, M. Joost, S. Kraft, F. Kroll, M. Kaluza, O. Kester, Z. Lecz, T. Merz, F. Nürnberg, H. Al-Omari, A. Orzhekhovskaya, G. Paulus, J. Polz, U. Ratzinger, M. Roth, G. Schaumann, P. Schmidt, U. Schramm, G. Schreiber, D. Schumacher, T. Stoehlker, A. Tauschwitz, W. Vinzenz, F. Wagner, S. Yaramyshev, and B. Zielbauer, Nucl. Instrum. Methods Phys. Res. Sect. A **740**, 94 (2014).
37. C. Brabetz, S. Busold, T. Cowan, O. Deppert, D. Jahn, O. Kester, M. Roth, D. Schumacher, and V. Bagnoud, Phys. Plasmas **22**, 013105 (2015).
38. J. Vieira, R. M. G. M. Trines, E. P. Alves, R. A. Fonseca, J. T. Mendonça, R. Bingham, P. Norreys, and L. O. Silva, Nat. Commun. **7**, 10371 (2016).
39. A. Denoeud, L. Chopineau, A. Leblanc and F. Quéré, Phys. Rev. Lett. **118**, 033902 (2017).
40. J. B. Ohland, D. Posor, U. Eisenbarth, V. Iancu, R. Ungureanu, D. Ursescu, and V. Bagnoud, High Power Laser Sci. Eng. **11**, e86 (2023).
41. L. Allen, M. W. Beijersbergen, R. J. C. Spreeuw, and J. P. Woerdman, Phys. Rev. A **45**, 8185 (1992).
42. X. Wang, Z. Nie, Y. Liang, J. Wang, T. Li, and B. Jia, Nanophotonics **7**, 1533 (2018).
43. Y. Shen, X. Wang, Z. Xie, C. Min, X. Fu, Q. Liu, M. Gong, and X. Yuan, Light Sci. Appl. **8**, 90 (2019).
44. M. Beijersbergen, L. Allen, H. van der Veen, and J. Woerdman, Opt. Commun. **96**, 123 (1993).
45. M. Beijersbergen, R. Coerwinkel, M. Kristensen, and J. Woerdman, Opt. Commun. **112**, 321 (1994).
46. R. Aboushelbaya, K. Glize, A. Savin, M. Mayr, B. Spiers, R. Wang, N. Bourgeois, C. Spindloe, R. Bingham, and P. Norreys, Phys. Plasmas **27**, 053107 (2020).
47. K. Sueda, G. Miyaji, N. Miyanaga, and M. Nakatsuka, Opt. Express **12**, 3548 (2004).
48. A. Longman and R. Fedosejevs, Opt. Express **25**, 17382 (2017).
49. J. B. Ohland, U. Eisenbarth, M. Roth, and V. Bagnoud, Appl. Phys. B **125**, 202 (2019).
50. A. Longman, C. Salgado, G. Zeraouli, J. I. Apiñaniz, J. Antonio Pérez-Hernández, M. K. Eltahlawy, L. Volpe, and R. Fedosejevs, Opt. Lett. **45**, 2187 (2020).
51. A. Longman and R. Fedosejevs, Phys. Plasmas **29**, 063109 (2022).
52. V. Bazhenov, M. Soskin, and M. Vasnetsov, J. Mod. Opt. **39**, 985 (1992).
53. A. S. Ostrovsky, C. Rickenstorff-Parrao, and V. Arrizón, Opt. Lett. **38**, 534 (2013).
54. Y. Chen, Z.-X. Fang, Y.-X. Ren, L. Gong, and R.-D. Lu, Appl. Opt. **54**, 8030 (2015).
55. F. Yue, D. Wen, J. Xin, B. D. Gerardot, J. Li, and X. Chen, ACS Photonics **3**, 1558 (2016).
56. L. Marrucci, C. Manzo, and D. Paparo, Phys. Rev. Lett. **96**, 163905 (2006).
57. M. Beresna, M. Gecevičius, and P. G. Kazansky, Opt. Mater. Express **1**, 783 (2011).
58. Z. Chen, S. Zheng, X. Lu, X. Wang, Y. Cai, C. Wang, M. Zheng, Y. Ai, Y. Leng, S. Xu, and D. Fan, High Power Laser Sci. Eng. **10**, e32 (2022).
59. S. Meimon, T. Fusco, and L. M. Mugnier, Opt. Lett. **35**, 3036 (2010).
60. C. Plantet, S. Meimon, J.-M. Conan, and T. Fusco, Opt. Express **21**, 16337 (2013).
61. A. Longman and R. Fedosejevs, J. Opt. Soc. Am. A **37**, 841 (2020).
62. A.-M. Talposi and D. Ursescu, J. Opt. Soc. Am. A **39**, 267 (2022).
63. A.-M. Talposi, V. Iancu, and D. Ursescu, Photonics **9**, 389 (2022).
64. I. J. Kim, J. Y. Bae, H. S. Kim, G. H. Kim, K. S. Chang, C. Jeon, I. W. Choi, and C. H. Nam, Patent US11947104 (2 April, 2024).

https://doi.org/10.1017/hpl.2024.59 Published online by Cambridge University Press